

## ARTICLE

## Chemical and Spectroscopic Characterization of Plutonium Tetrafluoride

Received 00th January 20xx,  
Accepted 00th January 20xx

DOI: 10.1039/x0xx00000x

Jared S. Kinyon<sup>a</sup>, Eliel Villa-Aleman\*<sup>a</sup> Elodia Ciprian<sup>b</sup>, Amy E. Hixon<sup>b</sup> Bryan J. Foley<sup>a</sup>, Jonathan H. Christian<sup>a</sup>, Jason R. Darvin<sup>a</sup>, Don D. Dick<sup>a</sup>, Amanda J. Casella<sup>c</sup>, Lucas E. Sweet<sup>c</sup>, Edgar C. Buck<sup>c</sup>, Forrest D. Heller<sup>c</sup>, Aaron D. Nicholas<sup>c</sup>, Cody A. Nizinski<sup>c</sup>, Richard A. Clark<sup>c</sup>

Anhydrous plutonium tetrafluoride is an important intermediate in the production of metallic Pu. This historically important compound is also known to exist in at least two distinct, yet understudied hydrate forms,  $\text{PuF}_4 \cdot x\text{H}_2\text{O}(s)$  ( $0.5 \leq x \leq 2$ ) and  $\text{PuF}_4 \cdot 2.5\text{H}_2\text{O}(s)$ . X-ray diffraction (XRD), thermogravimetric analysis (TGA), and scanning electron microscopy (SEM) are the most common tools used to characterize these materials, often in a context for studying structural and morphological changes that arise from aging or calcination. However, fundamental electronic and vibrational spectroscopic information is rather scarce. Here, we measured the visible and shortwave infrared (SWIR) diffuse reflectance, Fourier transform infrared (FTIR), fluorescence and Raman spectra of  $\text{PuF}_4(s)$  and  $\text{PuF}_4 \cdot x\text{H}_2\text{O}(s)$  to obtain a better electronic and vibrational fingerprint. Our work provides clear indication of the polymeric structure of anhydrous  $\text{PuF}_4$ , consistent with the Raman spectrum of  $\text{UF}_4(s)$  and its hydrates. This is supplemented with XRD, TGA and SEM analysis. Findings in this study indicate that the spectra are modified by particle size, which in turn is influenced by synthetic technique.

### Introduction

Since its discovery in 1940, plutonium (Pu) has held a unique position among the chemical elements. Though its destructive capabilities in nuclear weapons will live in infamy, plutonium and the chemical compounds that it forms are of fundamental importance for understanding the chemistry of the actinide series of elements. Despite this, chemical research on plutonium is relatively scarce compared to lighter actinides like uranium and thorium. This scarcity is largely due to a focus on the weaponization of Pu and is exacerbated by the health hazards and proliferation risks that are involved with handling and storing it.

In the early days of plutonium research - not long after Pu was discovered - most studies were application-centric, with a clear focus on maximizing production of Pu metal to develop nuclear arsenals. During this process, plutonium tetrafluoride ( $\text{PuF}_4(s)$ ) was discovered to be one of the first plutonium-containing compounds to have utility, leading to its original development during World War II as an intermediate for Pu metal production. Most early studies of anhydrous  $\text{PuF}_4$  were metallurgical in nature and focused on optimizing fluorination conditions [1] and engineering better metal recovery [2, 3], with a clear aim to

optimize production of Pu metal on an industrial scale [1-6]. This narrow focus of weaponizing Pu provided few opportunities to study the fundamental properties of Pu and its chemical compounds. However, this changed after the collapse of the Soviet Union in 1991, which shifted Pu-based research away from weaponization and towards nuclear waste management and nonproliferation.

To date, the preponderance of Pu-based chemical research has focused on  $\text{PuO}_2(s)$  due its prevalence in nuclear fuels [7-12] and waste storage [13]. By comparison, there is a dearth of modern studies pertaining to  $\text{PuF}_4$  [14-22]. This data gap is worsened by the structural instability of  $\text{PuF}_4$  and its hydrates. Many stockpiles of anhydrous  $\text{PuF}_4$  have degraded and become amorphous due to radiolytic decay, and most research facilities are no longer equipped to produce it, which is typically prepared by high temperature fluorination with highly corrosive HF gas [18]. However, such work is important to understand periodic trends and improve modelling of actinide chemistry. As a general rule, periodic trends for actinide elements are difficult to establish theoretically, which is why experimental techniques such as Raman, infrared (IR), diffuse reflectance, nuclear magnetic resonance (NMR), electron paramagnetic resonance (EPR) and X-ray photoelectron spectroscopies (XPS) are quite useful. Practically, their non-destructive nature has made them well-suited for characterizing materials of importance to the nuclear fuel cycle, such as  $\text{UF}_4$  and its hydrates [23-31],  $\text{PuO}_2$  [14, 32-41] and various forms of plutonium oxalate [14, 37-40, 42]. Without foundational experimental data, computational studies of Pu can be quite cumbersome [43-49].

<sup>a</sup> Savannah River National Laboratory; Aiken, SC, 29808.

<sup>b</sup> University of Notre Dame, Notre Dame, IN, 46556.

<sup>c</sup> Pacific Northwest National Laboratory; P.O. Box 999, Richland, WA 99352.

† Footnotes relating to the title and/or authors should appear here.

Supplementary Information available: [details of any supplementary information available should be included here]. See DOI: 10.1039/x0xx00000x

In this manuscript, we utilize vibrational spectroscopy, X-ray diffraction, microscopy, and thermogravimetric analysis to provide an exquisite look at the structure and morphology of  $\text{PuF}_4$  and  $\text{PuF}_4 \cdot x\text{H}_2\text{O}$ , thus filling a longstanding knowledge gap, elucidating important trends in the actinide series of elements, and providing new data to improve the accuracy of actinide computational models.

## Results and Discussion

### Structure and Morphology

The diffraction pattern of anhydrous  $\text{PuF}_4$  (Figure 1) is consistent with previous studies of  $\text{PuF}_4$  [18, 19] and isostructural to the anhydrous actinide fluorides  $\text{NpF}_4$  and  $\text{UF}_4$  [16, 50-52], both of which belong to the  $C2/c$  space group. Our pXRD data were initially fit to an  $\text{NpF}_4$  model [53] and the unit cell parameters were refined to adjust for the slightly smaller Pu atoms. Refined unit cell parameters are not reported due to the uneven surface from our sample preparation. Our analysis resulted in a cell volume that was  $14.82 \text{ \AA}^3$  smaller than  $\text{NpF}_4$ , which is not unreasonable given that  $\text{Pu}^{4+}$  is smaller than  $\text{Np}^{4+}$  [54]. A broad feature around  $15^\circ 2\theta$  was consistently measured in our  $\text{PuF}_4$  diffractograms but did not fit with our chosen structural model. This feature was not present in the diffraction pattern of the polyimide film that encased our sample. However, as our FTIR results show, this material is hygroscopic, which could explain the presence of this feature.

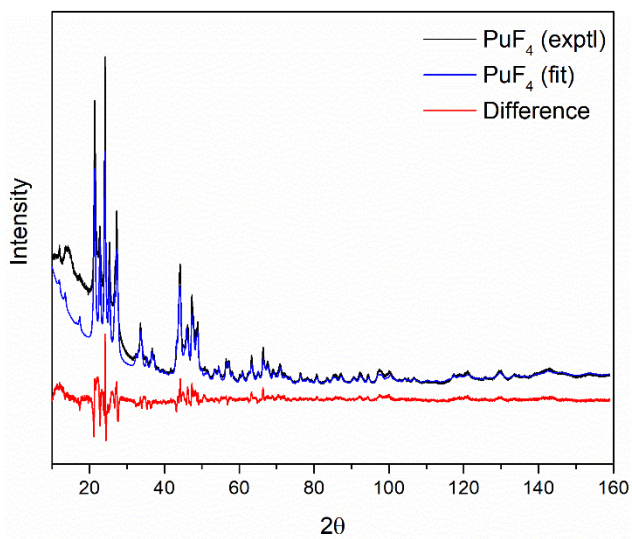


**Figure 1:** The observed pXRD pattern of anhydrous  $\text{PuF}_4$  (black) is compared to a fit diffraction pattern refined from the known  $\text{NpF}_4$  structure (blue), while the difference plot is shown in red.

In contrast, hydrated  $\text{PuF}_4$  is known to exist in at least two structurally distinct forms isostructural to the uranium variants—the simple cubic ( $\text{Fm}\bar{3}\text{m}$ ) and orthorhombic ( $\text{Pnma}$ ) geometries for  $\text{PuF}_4 \cdot x\text{H}_2\text{O}$  ( $0.5 \leq x \leq 2$ ) and  $\text{PuF}_4 \cdot 2.5\text{H}_2\text{O}$ , respectively [55-57]. The 2.5 hydrate is generally stable at room temperature, but infrared measurements have shown that weakly bound water molecules are likely responsible for the variability of  $x$  in the cubic form [26]. As shown in Figure 2, our

experimental diffractogram aligns with the published pattern reported by Dawson et al. (ICDD #00-034-0515) for the  $\text{PuF}_4 \cdot x\text{H}_2\text{O}$  structure [55]. From a chemical perspective, the relatively simple diffractogram seems rather curious, as  $\text{UF}_4 \cdot 0.33\text{H}_2\text{O}$  [27],  $\text{UF}_4 \cdot 1.33\text{H}_2\text{O}$  [58] and  $\text{UF}_4 \cdot 2.5\text{H}_2\text{O}$  [31, 59, 60] are all known to produce numerous diffraction bands that result from a complex structure.

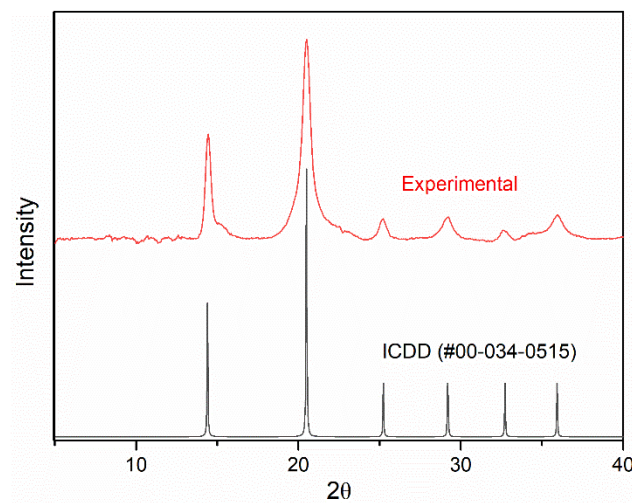


**Figure 2:** The experimental and ICDD (#00-034-0515) pXRD patterns of  $\text{PuF}_4 \cdot x\text{H}_2\text{O}$ .

To supplement these results, SEM measurements were conducted on both hydrated and anhydrous  $\text{PuF}_4$ . Micrographs of  $\text{PuF}_4 \cdot x\text{H}_2\text{O}$  (Figure 3) reveal that our material contained agglomerates of rounded submicron particles, though the limited resolution hindered a quantitative description of size. The aggregated morphology indicates rapid precipitation from solution, which is supported by earlier solubility experiments [61]. This was experimentally observed when our emerald-green  $\text{Pu}(\text{NO}_3)_4$  solution promptly turned light pink upon the addition of concentrated HF. Synthetic efforts, including cooling reagents, reducing HF concentration, and reducing the rate at which HF was added to  $\text{Pu}(\text{NO}_3)_4$ , were attempted to reduce the rate of  $\text{PuF}_4 \cdot x\text{H}_2\text{O}$  precipitation and produce larger particles. Unfortunately, these attempts were unsuccessful.

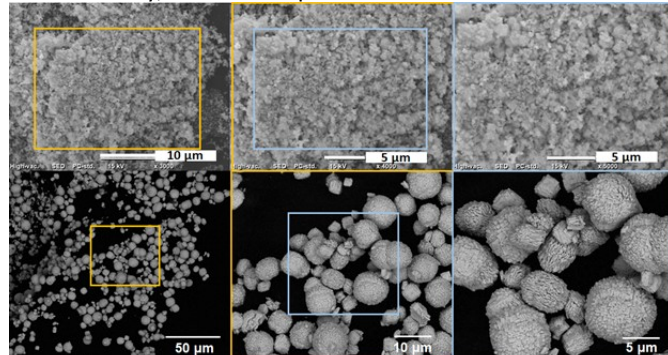


**Figure 3:** SEM-SE images of  $\text{PuF}_4 \cdot x\text{H}_2\text{O}$  (top) and SEM-CSE images of anhydrous  $\text{PuF}_4$  (bottom) at increasing magnification.

In contrast, anhydrous  $\text{PuF}_4$  possessed larger particle sizes ranging from 5-10  $\mu\text{m}$  in diameter. The particle surfaces were rough with pits and layered edges; such features have been

observed after the calcination of Pu(IV) oxalate to  $\text{PuO}_2$  [38]. Elemental analysis of the material showed no evidence of discrete Pu or F rich regions. However, the anhydrous images (Figure 3) are quite distinct from those reported on an aged powder produced at Los Alamos National Laboratory (LANL), which primarily consisted of crystalline aggregates 5-20  $\mu\text{m}$  in length along their longest dimension [19]. The differing morphologies likely originate from the precipitation and calcination steps, both of which have been shown to affect the size of  $\text{PuO}_2$  particulates [62-65].

TGA was used to measure the mass loss of freshly synthesized  $\text{PuF}_4\cdot\text{xH}_2\text{O}$  during heating (Figure 4a). A total weight loss of 6.54 wt. % was observed when heated to 800  $^{\circ}\text{C}$  under nitrogen. An initial weight loss of 5.4 wt. % occurred from room temperature to 410  $^{\circ}\text{C}$  and is attributed to water removal, which could ostensibly originate from the lattice or surface-adsorbed molecules. For a pure lattice contribution, this would correspond with  $x = 1$ , which is consistent with pXRD results. Additionally, the dehydration is similar to what has been observed for anhydrous  $\text{PuF}_4$  with an 8%  $\text{PuF}_4\cdot 1.6\text{H}_2\text{O}$  crystalline phase [19]. The remaining 1.1 wt. % loss at 800  $^{\circ}\text{C}$  is assigned to the removal of weakly coordinated fluorine, which has been shown by both Wayne et al. and Dawson et al. to occur between 300 and 450  $^{\circ}\text{C}$  [19, 55]. Another possibility for the remaining mass loss could result from the reaction of  $\text{PuF}_4$  and  $\text{PuO}_2$  to produce  $\text{O}_2$  and  $\text{PuF}_3$  [19, 66].

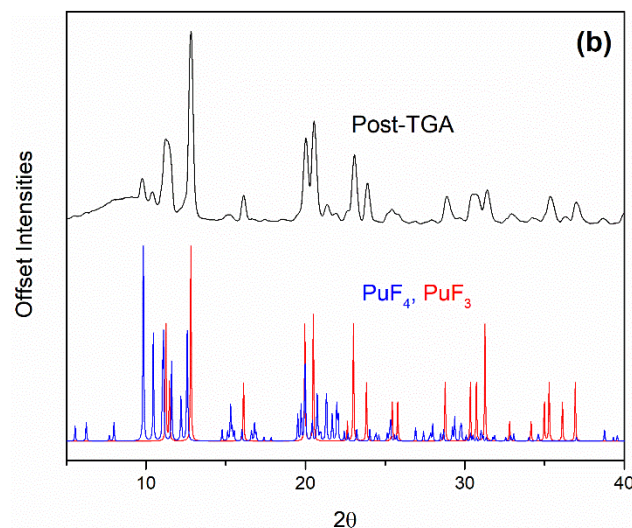
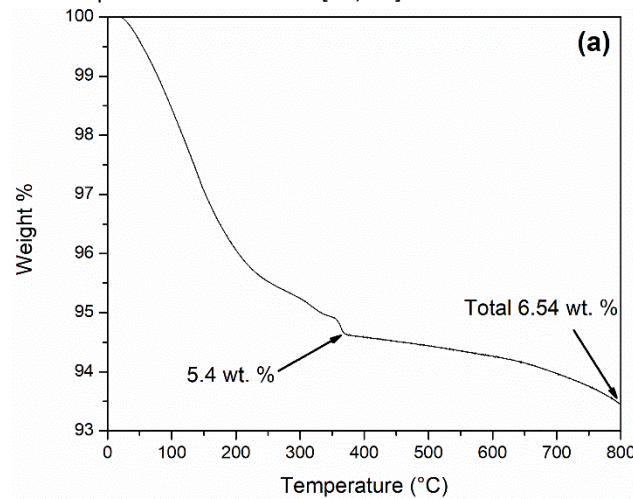


**Figure 4:** (a) Thermal decomposition of  $\text{PuF}_4\cdot\text{xH}_2\text{O}$  under nitrogen heated to 800  $^{\circ}\text{C}$  at a ramp rate of 5  $^{\circ}\text{C}/\text{min}$ . (b) ICDD patterns for  $\text{PuF}_4$  (#00-041-1218, blue) and  $\text{PuF}_3$  (#00-006-0327, black) in comparison to post-TGA  $\text{PuF}_4\cdot\text{xH}_2\text{O}$ .

The production of both  $\text{PuF}_4$  and  $\text{PuF}_3$  at high temperatures is further supported by pXRD results of the post-TGA  $\text{PuF}_4\cdot\text{xH}_2\text{O}$  (Figure 4b). This is an important observation, as previous literature work on this matter is unclear. For example, under vacuum at  $10^{-4}$  Torr, Dawson et al. observed a  $\text{PuF}_3$  and  $\text{PuF}_4$  mixture when  $\text{PuF}_4\cdot\text{xH}_2\text{O}$  is heated to 550  $^{\circ}\text{C}$ . For a second sample under vacuum Dawson et al. reported  $\text{PuF}_3$  and  $\text{PuO}_2$  when heating to 900  $^{\circ}\text{C}$  [56]. The same products were produced for a hydrate when heated to 300  $^{\circ}\text{C}$  in an  $\text{N}_2$  atmosphere [55]. It was suggested that dehydrated  $\text{PuF}_4$  could react with liberated water to produce  $\text{PuO}_2$ , which in turn reacts with  $\text{PuF}_4$  to produce  $\text{PuF}_3$ . In contrast, Wayne et al. did not observe the formation of  $\text{PuF}_3$ ; this is likely due to the use of open crucibles under an Ar atmosphere, which didn't allow for back-reaction with evolved gases [19].  $\text{PuO}_2$  has also been reported as a byproduct of heating  $\text{PuF}_4\cdot\text{xH}_2\text{O}$  above 300  $^{\circ}\text{C}$  in vacuum or dry nitrogen [19, 55], though its presence can usually be attributed to crystalline impurities inherent to the sample [18, 19]. No impurities were found in our sample; however, it is possible undetected impurities reacted with  $\text{PuF}_4$ .

#### Raman Spectroscopy

For the first time, Raman spectroscopy was used to elucidate the structures of  $\text{PuF}_4$  and  $\text{PuF}_4\cdot\text{xH}_2\text{O}$ . Generally, it is challenging to measure high-quality spectra for metal fluorides because the intensity of Raman bands depend on bond polarizability, and metal-fluorine bonds are weakly polarizable. Fluorescence complicates matters, and has been shown to further obscure signals from  $\text{UF}_4\cdot 0.33\text{H}_2\text{O}$ ,  $\text{U}_3\text{F}_{12}\cdot\text{H}_2\text{O}$ , and  $\text{UF}_4\cdot 2.5\text{H}_2\text{O}$  [24, 27, 31]. We worked under the assumption that both  $\text{PuF}_4$  and its hydrate possess a complex polymeric structure, similar to  $\text{UF}_4$  and  $\text{UF}_4\cdot 2.5\text{H}_2\text{O}$  [50, 59, 67].

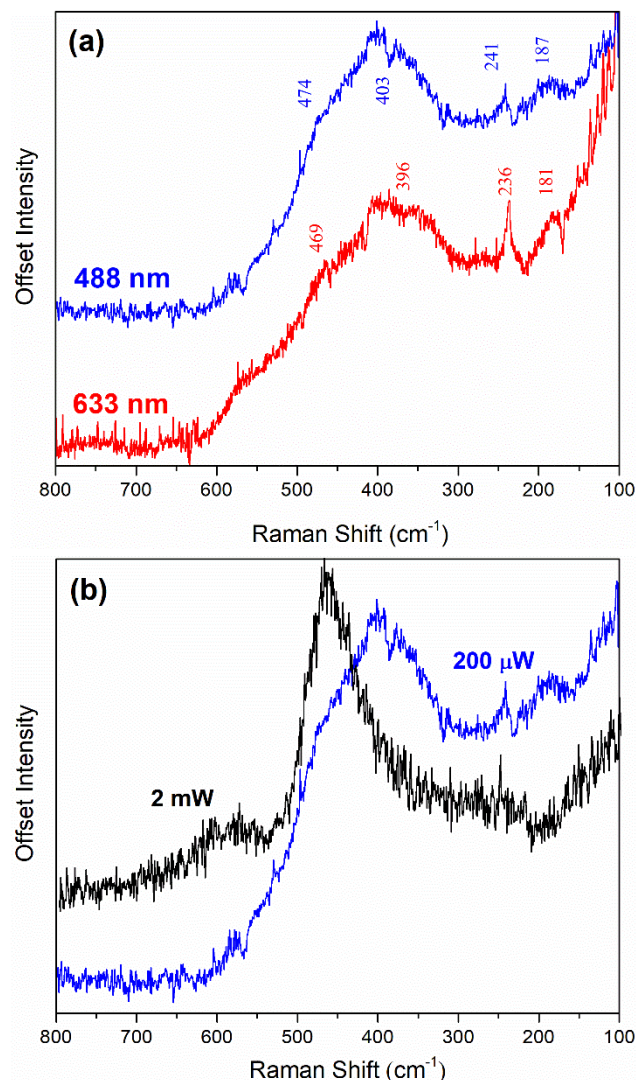


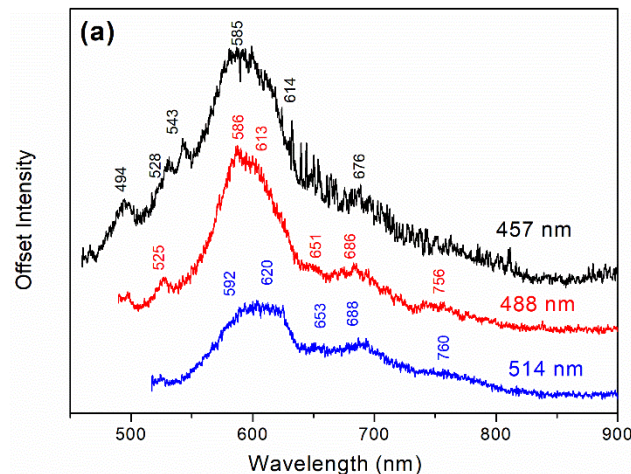
**Figure 5:** (a) Raman spectra of  $\text{PuF}_4 \cdot x\text{H}_2\text{O}$  measured at 488 nm (blue) and 633 nm (red). (b) The 488 nm spectrum (blue) measured at 200  $\mu\text{W}$  compared to another measured at 2 mW (black). Both plots are given a dual y-axis (intensities) for the convenient comparison of spectral features.

The Raman spectrum of  $\text{PuF}_4 \cdot x\text{H}_2\text{O}$  (Figure 5a) primarily features a broad band centered around  $400 \text{ cm}^{-1}$  and several low intensity bands. The broad feature around  $400 \text{ cm}^{-1}$  likely results from the small particle morphology of  $\text{PuF}_4 \cdot x\text{H}_2\text{O}$ , as Raman spectra can be affected by phonon confinement [68] leading to broad, asymmetric band shapes. Thus, our Raman measurements corroborate the SEM findings.

Two challenges were encountered when measuring the Raman spectrum of  $\text{PuF}_4 \cdot x\text{H}_2\text{O}$ . First, naturally weak Raman scattering could not be enhanced by increasing laser power since the material was susceptible to decomposition and oxidation upon heating, even with long-term exposure to a low-powered laser. This is unsurprising, as submicron particles are known to undergo laser heating at powers as low as 1 mW. This phenomenon is shown in Figure 5b. At 2 mW, our samples of  $\text{PuF}_4 \cdot x\text{H}_2\text{O}$  had thermally decomposed to  $\text{PuO}_2$  nanoparticles, as evidenced by the observation of a broad ( $\text{FWHM} = 20 \text{ cm}^{-1}$ )

band centered at  $465 \text{ cm}^{-1}$ , with a weaker shoulder centered near  $600 \text{ cm}^{-1}$ . Typically,  $\text{PuO}_2$  calcined at  $450^\circ\text{C}$  displays a relatively sharp band at  $476 \text{ cm}^{-1}$  and a broad, weak band at  $580 \text{ cm}^{-1}$  which correspond to the  $\text{T}_{2g}$  (1LO1) and 1LO2 bands of  $\text{PuO}_2$ , respectively [32-35, 69, 70]. In this case, the FWHM broadening and shift to lower frequencies can be explained by phonon confinement effects and crystallite dimensions of less than 10 nm. Consequently, very low laser powers ( $< 250 \mu\text{W}$ ) and long acquisition times were employed to avoid conversion of both  $\text{PuF}_4$  and  $\text{PuF}_4 \cdot x\text{H}_2\text{O}$  to  $\text{PuO}_2$ .

The second challenge with measuring the Raman spectrum of  $\text{PuF}_4 \cdot x\text{H}_2\text{O}$  is wavelength-dependent fluorescence, which obscures vibrational modes. To determine which spectral features were Raman bands and which were fluorescence, the Raman spectrum of  $\text{PuF}_4 \cdot x\text{H}_2\text{O}$  was measured at 457, 488, 514, and 633 nm laser excitation wavelengths. Spectral features that were reproducible at different excitation wavelengths were labeled and assigned as Raman bands in Figure 5a, while those shifted in position with respect to excitation wavelength were ascribed to fluorescence (Figure 6a). Raman bands for  $\text{PuF}_4 \cdot x\text{H}_2\text{O}$  were located near 187, 240, 403 and 474  $\text{cm}^{-1}$ , which are in the same spectral region as  $\text{UF}_4$  metal-fluorine bands ( $70 \text{ cm}^{-1}$  to  $650 \text{ cm}^{-1}$ ). These low intensity peaks were superimposed on a baseline rising towards the laser excitation wavelength; it is likely that this effect arises ostensibly not from fluorescence, but the significant number of low-frequency modes originating from F-F polymeric interactions and hydrogen bonding from water. Such observations have been made for  $\text{UF}_4$  and  $\text{UF}_4 \cdot 2.5\text{H}_2\text{O}$  [24, 31].



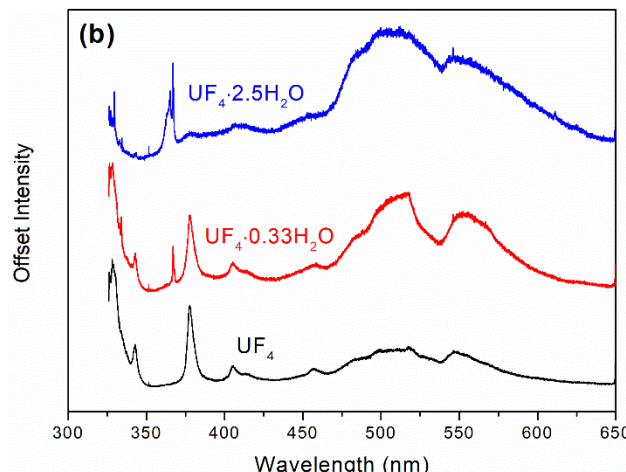


**Figure 6:** (a) Fluorescence spectra of  $\text{PuF}_4\text{-xH}_2\text{O}$  measured with 457 (black), 488 (red), and 514 (blue) nm excitation wavelengths, with respective powers of 444, 172 and 172  $\mu\text{W}$ . (b) Unpublished fluorescence spectra of  $\text{UF}_4$  (black),  $\text{UF}_4\text{-}0.33\text{H}_2\text{O}$  (red) and  $\text{UF}_4\text{-}2.5\text{H}_2\text{O}$  (blue) taken at 325 nm.

Figure 6a and Table 1 show the fluorescence spectrum and peak positions, respectively, for  $\text{PuF}_4\text{-xH}_2\text{O}$  at 457, 488, and 514 nm. The large number of fluorescent features is quite interesting as fluorescent signatures are often used to rapidly assess chemical composition in nuclear forensics, such as for  $\text{UF}_4$  particulates [24, 71]. Fluorescence spectra collected at different wavelengths possessed a common peak and weak shoulder centered near 600 and 685 nm, respectively. The independence of overall band structure with excitation wavelength indicates that these peaks result from electronic transitions, as would be expected from the Vavilov rule. Larger energy transitions, observed at 457 and 488 nm, may have originated from otherwise inaccessible vibronic states.

**Table 1:** Fluorescent bands (nm) observed for  $\text{PuF}_4\text{-xH}_2\text{O}$  as a function of laser excitation wavelength (nm).

Fluorescent Spectral Bands			
Excitation	457	488	514
Bands	494		
	528	525	
	543		
	585	586	592
	614	613	620
		651	653
	676	686	688
		756	760

Fluorescence generally indicates a preferred relaxation path for excited energy levels. As shown in Figure 6b,  $\text{UF}_4$  and its hydrates have many identical features. This strongly suggests that the origin of the signal is based on the electronic states of U(IV), remaining largely uncoupled from its molecular structure.

By analogy, we hypothesize that the fluorescence observed for  $\text{PuF}_4\text{-xH}_2\text{O}$  arises from different electronic transitions of Pu(IV). The relative strength of the fluorescence bands relative to the Raman could help in the detection and analysis of  $\text{PuF}_4\text{-xH}_2\text{O}$ .

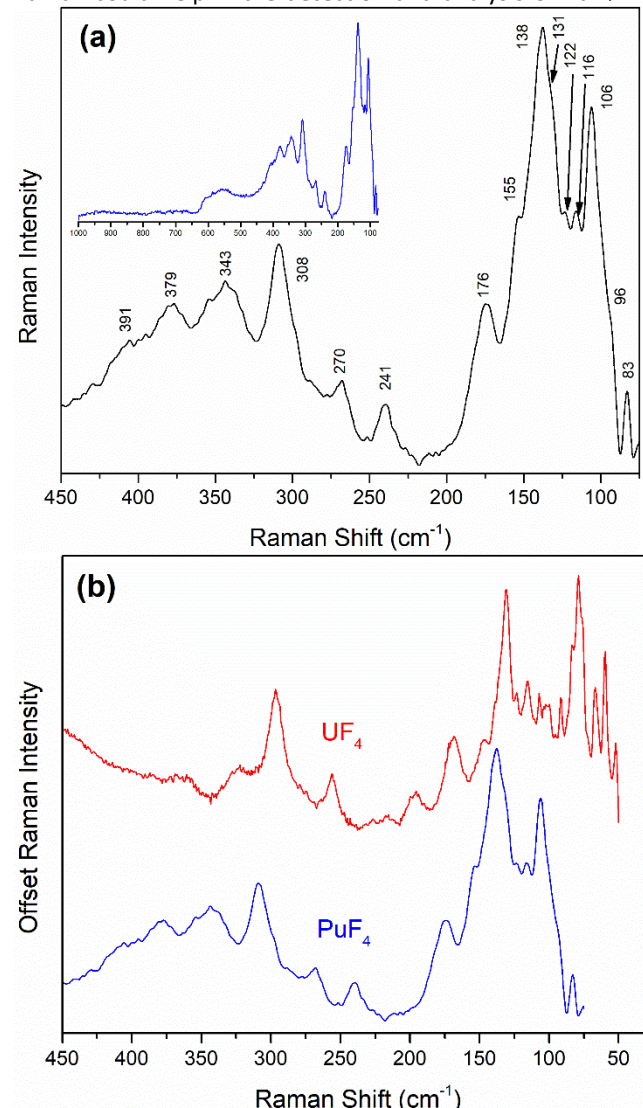


**Figure 7:** (a) Raman spectrum of anhydrous  $\text{PuF}_4$  measured with an excitation wavelength of 514 nm with bands labeled in the region of interest. The blue inset displays the full spectral range from 50–1000  $\text{cm}^{-1}$ . (b) A comparison of the anhydrous variants of  $\text{UF}_4$  (red) [24] and  $\text{PuF}_4$  (blue) Raman spectra taken at 514 nm. Plot is given a dual y-axis for convenient comparison of spectral features.

The Raman spectrum of anhydrous  $\text{PuF}_4$  (Figure 7) was markedly different than  $\text{PuF}_4\text{-xH}_2\text{O}$  and allowed for a more direct comparison with previously published spectra for  $\text{UF}_4$ . As shown in Figure 3, anhydrous  $\text{PuF}_4$  particles were much larger than  $\text{PuF}_4\text{-xH}_2\text{O}$ , which prevented phonon confinement and spectral broadening. Further, the larger particles of  $\text{PuF}_4$  were less susceptible to laser-induced heating during Raman measurements, enabling spectral acquisition using a laser power of up to 500  $\mu\text{W}$ , as opposed to 250  $\mu\text{W}$  for  $\text{PuF}_4\text{-xH}_2\text{O}$ . However, long term exposure to laser power still results in the formation of  $\text{PuO}_2$ , as it does for the hydrate. This work has

identified at least 15 Raman bands between 50  $\text{cm}^{-1}$  and 400  $\text{cm}^{-1}$  and are listed in Table 2. As shown in Figure 7b, the spectra of  $\text{PuF}_4$  and  $\text{UF}_4$  share many similarities. The numerous bands in the low frequency region are typical for a fluorine polymeric structure dominating a Raman spectrum [24, 27, 28, 31] and cannot be modeled on the basis of a tetrahedral monomer surrounding Pu [67].

**Table 2:** Raman spectral bands for  $\text{PuF}_4$  and  $\text{PuF}_4\text{-xH}_2\text{O}$ , as labeled in Figure 5, are compared to bands previously measured for  $\text{UF}_4$  [24] and  $\text{UF}_4\text{-0.33H}_2\text{O}$  [27]. Save for the cubic  $\text{PuF}_4\text{-xH}_2\text{O}$ , the crystallographic structures are all similar and belong to  $\text{C}2/\text{c}$ .

Raman Spectral Bands			
$\text{UF}_4$	$\text{PuF}_4$	$\text{UF}_4\text{-0.33H}_2\text{O}$	$\text{PuF}_4\text{-xH}_2\text{O}$
		50.9	
59.4			
66.8		61.7	
78.9	82.7	76.6	
		84.8	603.6
91	96.3		
		93.3	637
		96.8	3532
101.3		102	3602
107.2	105.8	108	
115.9	116.2	118	
		122.5	
131.4	130.6	132	
	138.1	141	
148.5			

**Table 3.** These measurements are interesting since most infrared measurements on solid-state Pu(IV) samples are limited [38, 42, 72, 73], with most of literature focusing on the analysis of aqueous solutions in the presence of species such as  $\text{ClO}_4^-$ ,  $\text{Cl}^-$ ,  $\text{NO}_3^-$  and  $\text{HNO}_3$  [74].

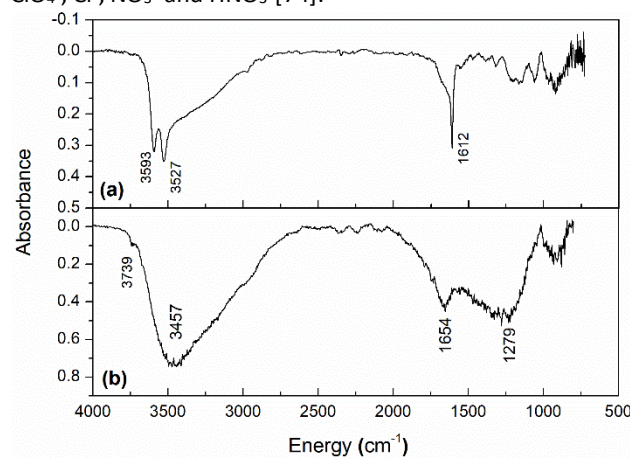


**Figure 8:** Room-temperature FTIR spectra of (a) anhydrous  $\text{PuF}_4$  and (b)  $\text{PuF}_4\text{-xH}_2\text{O}$  taken at room temperature.

Generally, Actinide-fluoride bonds are not expected to possess IR active modes at frequencies greater than 500  $\text{cm}^{-1}$ . This is

155.1			
170.4	175.6	175	187
197.3			236
	240.7		241
255.8			
	270.2		
296.1			
	307.7	307	
322.4			
	332		
	342.5		
360.8		363	403
	378.5	382	474
	391		

### Infrared Spectroscopy

FTIR was used to gain a more complete picture of the vibrational modes of the water molecules absorbed in  $\text{PuF}_4$  and  $\text{PuF}_4\text{-xH}_2\text{O}$  and are shown in Figure 8, while the peak positions are listed in

best reflected by the FTIR spectrum of anhydrous  $\text{UF}_4$ , which has been shown to have no active vibrational mode between 500–4000  $\text{cm}^{-1}$  [31]. This result is supported by DFT calculations, which predicted no IR-active modes for  $\text{UF}_4$  above 400  $\text{cm}^{-1}$  [23]. Therefore, it is expected that the peaks for  $\text{PuF}_4\text{-xH}_2\text{O}$  and  $\text{PuF}_4$  displayed in Figure 8 are related to water, OH stretches and low-frequency modes. The water band features in the anhydrous spectrum suggests either the presence of natural impurities (e.g., a small contribution of  $\text{PuF}_4\text{-xH}_2\text{O}$  within the anhydrous lattice) or an active sorption process, presumably from adsorbed water molecules or an isostructural hydrate with  $x < 0.5$ .

The sharp bands at 3593  $\text{cm}^{-1}$  and 3527  $\text{cm}^{-1}$  observed in the anhydrous spectrum of  $\text{PuF}_4$  (Figure 8a) are superimposed on a broad band indicative of free OH experiencing different chemical environments within the crystal lattice [31], while the broad band itself suggests the presence of hydrogen bonding and polymeric fluorine bonding modes. The long tail from hydrogen/fluorine bonding has been observed in IR spectra of  $\text{UO}_2\text{F}_2\text{-}(\text{H}_2\text{O})_x\text{(HF)}_y$  [75–78] and water with significant HF interactions [79]. The asymmetry of the OH region likely results from broad, overlapping hydrogen-bonded OH peaks in slightly different chemical environments [31]. Similar spectral features have been observed for  $\text{UF}_4\text{-0.33H}_2\text{O}$  [27] and  $\text{UF}_4\text{-2.5H}_2\text{O}$  [31].

Multiple peaks likely arise from OH groups weakly interacting with oxygen or fluorine neighbors.

At  $1612\text{ cm}^{-1}$ , there is another sharp peak overlayed on a weak asymmetric feature. The sharp band suggests an HOH bending mode in a specific configuration, while the weak broader asymmetrical component could be evidence of HOH bending in multiple chemical environments. A comparison to IR data from Khanaev et al. [26] suggests that  $\text{PuF}_4\cdot0.33\text{H}_2\text{O}$  may have been the hydrate in the sample prepared at PNNL and analyzed at SRNL. Though the means of  $\text{H}_2\text{O}$  introduction to the sample remains unknown, it can be noted that  $\text{PuF}_4$  was synthesized in the arid environment in which PNNL is located. It is possible that anhydrous  $\text{PuF}_4$  absorbed most of the water once exposed to

**Table 3** compares our results to the  $x = 2.3$  and  $x = 0.3$  variants. The sharp shoulder peak at  $3739\text{ cm}^{-1}$  is likely related to a free OH functional group; these usually have limited interactions with fluorine or water due to steric effects, resulting in sharper, higher-frequency bands with a FWHM  $< 50\text{ cm}^{-1}$  when compared with more strongly interacting OH groups. This contrasts with the broad, lower frequency peak at  $3457\text{ cm}^{-1}$  seen in  $\text{PuF}_4\cdot\text{xH}_2\text{O}$ , which is much more typical for a hydrogen-bonded OH group [27]. Finally, an HOH bending mode common for hydrated lattices can be observed at  $1654\text{ cm}^{-1}$  [26, 27].

**Table 3:** FTIR peaks for  $\text{PuF}_4$  and its hydrate. A comparison to peaks from the literature for  $\text{UF}_4\cdot0.33\text{H}_2\text{O}$ ,  $\text{PuF}_4\cdot2.3\text{H}_2\text{O}$  and  $\text{PuF}_4\cdot0.3\text{H}_2\text{O}$  is given for convenience. Experimental peaks are labeled in Figure 8.

	$\text{UF}_4\cdot0.33\text{H}_2\text{O}$ [27]	$\text{PuF}_4\cdot2.3\text{H}_2\text{O}$ [26]	$\text{PuF}_4\cdot0.3\text{H}_2\text{O}$ [26]	$\text{PuF}_4\cdot\text{xH}_2\text{O}$	$\text{PuF}_4$
O-H	3589			3739	3595
	3518	3525			3527
	3431	3375	3280	3457	
	3237	3200			
$\text{H}_2\text{O}$			1725		
			1705		
	1608	1650		1654	1612
	1556	1629	1632		
?				1279	
			789		
O-H*			769		
			650		
$\text{H}_2\text{O}/\text{F}$	427	560	560		
		480	490		
		440	445		
		400	400		
An-F					

### Diffuse Reflectance Spectroscopy

Diffuse reflectance spectroscopy (DRS) is a useful tool for analyzing the local electronic structure of actinides, including plutonium tetrafluoride. While both Raman and infrared spectroscopy help elucidate local site symmetry, DRS is advantageous because of its sensitivity to electronic metal–

ligand interactions. This allows it to provide detailed information based on the splitting of Laporte-forbidden  $ff$  transitions due to the influence of the crystal field [14, 15, 80–82], making it highly sensitive to changes in the lattice symmetry resulting from alterations to oxidation state or structure [83]. Its immunity to fluorescence, which often stymies the acquisition of Raman spectra, makes it an attractive technique.

The peaks for  $\text{PuF}_4\cdot\text{xH}_2\text{O}$  (Figure 8b) are related to water molecules in different chemical environments corresponding to OH stretches,  $\text{H}_2\text{O}$  bending modes and low-frequency modes. FTIR data has been described in detail for  $\text{PuF}_4\cdot\text{xH}_2\text{O}$  ( $x=2.3, 0.9, 0.6$  and  $0.3$ ) and closely matches the results from our material [26].

Comparisons with the  $\text{UF}_4$  hydrates strongly suggest that the water/ $\text{PuF}_4$  ratios are higher for  $\text{PuF}_4\cdot\text{xH}_2\text{O}$  than for  $\text{UF}_4\cdot2.5\text{H}_2\text{O}$  [31]. Though this would contradict the TGA results, the hydrated  $\text{PuF}_4$  structure is based on submicron particulates and likely affected by surface properties. Considering this, it is very likely that this sample could have sorbed water between measurements.

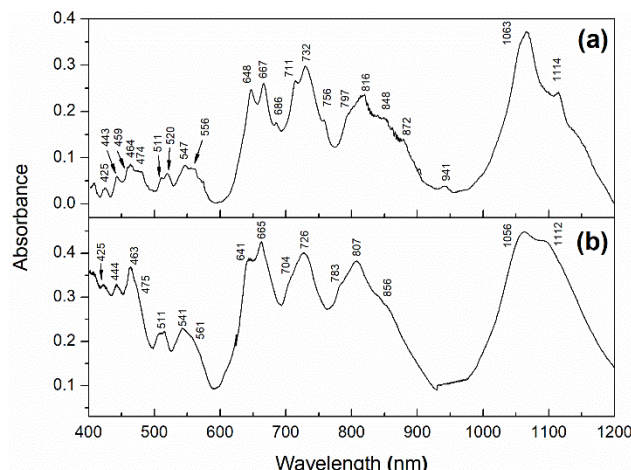


**Figure 9:** DRS spectra in the visible and shortwave infrared (SWIR) of (a)  $\text{PuF}_4$  and (b)  $\text{PuF}_4 \cdot x\text{H}_2\text{O}$  taken at room temperature.

The room-temperature DRS spectra for both  $\text{PuF}_4$  and  $\text{PuF}_4 \cdot x\text{H}_2\text{O}$  are displayed in Figure 9. These measurements are significant, as the available modern literature for diffuse reflectance on solid-state Pu complexes is limited, focusing instead on Pu-based coordination complexes arising from aqueous solvents [84-86], organic solvents [87-92], ionic liquids [93] and solid-state melts [94]. In the solid state, the primary interest in DRS has been to investigate the solubility and oxidative stability of Pu(IV) in solid matrices to assess their suitability for waste storage [95-98]. Only recently have the oxalates and oxides been scrutinized with modern instrumentation [37, 86].

Each spectrum features a complex combination of several relatively broad and sharp features from 400–1200 nm. Despite their known differences in crystallographic symmetry, many of the spectral features and positions of  $\text{PuF}_4 \cdot x\text{H}_2\text{O}$  were shared with anhydrous  $\text{PuF}_4$ , with the primary difference being in the broadness of the peaks, especially below 600 nm. The presence of water in the hydrate allows for greater overlap between the electronic bands resulting in peak broadening. The broadening of peaks observed in the hydrate could also be reflective of our SEM and XRD results; given that it is more amorphous than  $\text{PuF}_4$ , and that DRS is sensitive to the degree of crystallinity, the DRS spectrum of the hydrate should be expected to possess broader peaks than the anhydrous variant. The relative intensity increases for the hydrate peaks, such as at 464 and 1114 nm are not currently understood, but could be explained by changes in the local symmetry, since the crystal-field plays an important role in transition probability.

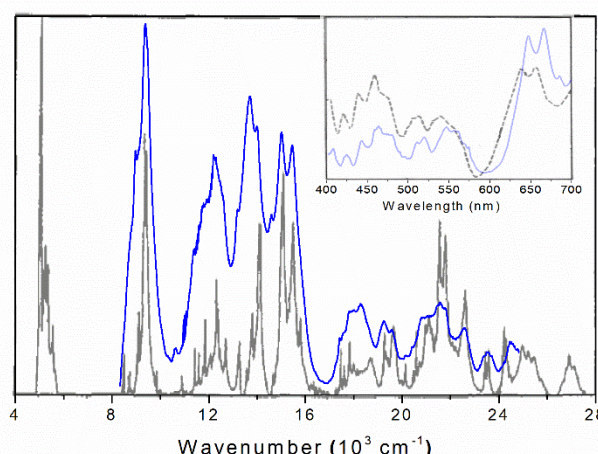


**Figure 10:** DRS spectra of anhydrous  $\text{PuF}_4$  at room temperature (blue), compared with its absorbance measured at 4 K (black, reproduced from [15] with the permission of AIP Publishing). The inset depicts another comparison of our  $\text{PuF}_4$  DRS spectrum to an earlier one made at room temperature [14].

Though not exhaustive, the DRS peaks are listed in **Table 4** and compared to literature values. This includes the room-temperature DRS spectrum of plutonium tetrafluoride measured by Hobart et al. for a presumably anhydrous sample from 400–700 nm [14] and is shown in the inset of Figure 10. The spectral features in the measured range match well, indicating no changes to the oxidation state of Pu(IV). The offset in peak position could be attributed to calibration issues. Given that the peak positions/intensities best match anhydrous  $\text{PuF}_4$  rather than  $\text{PuF}_4 \cdot x\text{H}_2\text{O}$ , our work clarifies that the original measurement was likely performed on an anhydrous sample. We also identified an additional peak at 686 nm and extended the range of the original measurement.

Also worth mentioning is the experimental work of Carnall et al. [15] measured the absorbance spectrum of anhydrous  $\text{PuF}_4$  pressed into a KBr pellet at 4 K from 360–2500 nm. Although band intensities might somewhat differ between absorbance and diffuse reflectance spectra, both provide the same information with regard to peak position and serves as a useful point of reference for the interpretation of our experimental results. Additionally, the low temperature of the measurement reduced spectral crowding and allowed for the identification of ground-state transitions. As seen in Figure 10, there is good agreement in the absorption spectrum and our DRS results; peaks with similar central positions are listed in **Table 4**. Lower temperature measurements would be expected to cause further sharpening and splitting of the room temperature peaks.

**Table 4:** Experimentally-determined DRS peak positions for anhydrous  $\text{PuF}_4$  and  $\text{PuF}_4 \cdot x\text{H}_2\text{O}$ . For convenience, these are compared to previously measured values for plutonium tetrafluoride, with *italic* values being estimates based on the provided literature plots in Figure 10. The degree of hydration for literature samples is unclear, and many of the sharper

splittings visible only at low temperatures are not included for brevity.

PuF <sub>4</sub> [14]	PuF <sub>4</sub> [15]	PuF <sub>4</sub>	PuF <sub>4</sub> ·xH <sub>2</sub> O
421	426	425	
440		443	444
	459		
460	464	464	463
470	473	474	475
506	509	511	511
513	519	520	
540	534	547	541
551	562	556	561
	572	574	
638	645	648	641
656	663	667	665
		686	
	710	711	704
	724	732	726
	753	756	
	788	797	783
	808	816	807
	826		
	842	848	856
	860		
	873	872	
	921	941	
	1060	1063	1056
	1093		
	1114	1112	
	1170		

## Conclusions

The crystallinity, morphology and optical properties of anhydrous PuF<sub>4</sub> and one of its hydrates, PuF<sub>4</sub>·xH<sub>2</sub>O, were studied with a variety of spectroscopic and microscopic techniques. Initial pXRD results showed a few peaks for PuF<sub>4</sub>·xH<sub>2</sub>O, as opposed to the more complex diffractogram expected for anhydrous PuF<sub>4</sub> or the other hydrate, PuF<sub>4</sub>·2.5H<sub>2</sub>O. These results were augmented by SEM, which provided a clear difference in particulate dimensions prepared from the dry and wet methods. In particular, the wet method showed preferential submicron particulate formation of PuF<sub>4</sub>·xH<sub>2</sub>O resulting from rapid precipitation, in stark contrast to the large PuF<sub>4</sub> agglomerates produced via dry synthesis. Additionally, TGA and post-XRD measurements clarified that the majority of mass lost from heating PuF<sub>4</sub>·xH<sub>2</sub>O occurs due to dehydration of the hydrate; an assumption of pure bonding and negligible adsorption would lead to an estimate of x = 1, which is consistent with pXRD results. The presence of PuF<sub>3</sub> above 800°C likely arises from the closed, non-oxidizing atmosphere of the TGA.

For the first time, the Raman spectra of both PuF<sub>4</sub> and PuF<sub>4</sub>·xH<sub>2</sub>O were recorded with several wavelengths. In particular, the spectrum of PuF<sub>4</sub>·xH<sub>2</sub>O was found to produce a poor signal, even when compared to UF<sub>4</sub> and its hydrates. In addition to weak polarizability, broad bands and a rising baseline made interpretation quite difficult. A rising baseline likely arises from F-F agglomerates and hydrogen bonding from water, whereas peak broadness can be explained by phonon confinement of the small particulates. In contrast, anhydrous PuF<sub>4</sub> had a much stronger response with sharper, well-defined Raman bands. Their spectral location closely mirrors UF<sub>4</sub>, representing a set of isostructural compounds (UF<sub>4</sub>, CeF<sub>4</sub>, etc.) where F-F vibrational modes dominate the Raman spectrum. The fluorescence spectra of PuF<sub>4</sub>·xH<sub>2</sub>O was also investigated and found to have bands analogous to those observed from UF<sub>4</sub> and its hydrates, suggesting the presence of electronic transitions that could be used to identify PuF<sub>4</sub> and its hydrates.

The water content was found to clearly impact the IR spectrum of both anhydrous PuF<sub>4</sub> and PuF<sub>4</sub>·xH<sub>2</sub>O at higher energies, especially since no metal-fluoride peaks were expected below 500 cm<sup>-1</sup>. Bands corresponding to water bending or OH stretch modes in dry PuF<sub>4</sub> suggest that water was sorbed during synthesis at PNNL or during handling in the humid environment at SRNL. Finally, DRS in the visible and shortwave infrared for both anhydrous PuF<sub>4</sub> and PuF<sub>4</sub>·xH<sub>2</sub>O closely match earlier literature reports for PuF<sub>4</sub>. Save for peak broadening in PuF<sub>4</sub>·xH<sub>2</sub>O, the almost matching spectra indicate that excess water does not affect the electronic interactions between fluoride and Pu(IV) ions.

## Experimental

### Synthesis

All plutonium syntheses were performed inside Hazard Category II nuclear facilities that permit the safe handling of weapons-grade (WG) plutonium (>93% <sup>239</sup>Pu). Anhydrous PuF<sub>4</sub> was prepared at Pacific Northwest National Laboratory (PNNL) by first purifying WG Pu(IV) nitrate using anion exchange chromatography. The purified Pu was then precipitated as Pu(IV) oxalate through addition of oxalic acid. The oxalate was then calcined to PuO<sub>2</sub> in air at 300 °C. The resulting PuO<sub>2</sub> was then converted to PuF<sub>4</sub> by reaction with anhydrous HF gas using the experimental set-up described by Casella et al.[21]. Briefly, PuO<sub>2</sub> was heated to 300 °C in an air/O<sub>2</sub> mixture. The atmosphere was then converted to an HF/O<sub>2</sub> mixture, and the temperature was increased and held at 480 °C for 2 hours. The final product had a light pink color that was consistent with previous descriptions of PuF<sub>4</sub>. The product was subsequently analyzed by powder X-ray diffraction (pXRD) to determine purity and reaction yield.

A hydrated sample of PuF<sub>4</sub>, henceforth referred to as PuF<sub>4</sub>·xH<sub>2</sub>O, was synthesized via low-temperature hydrofluorination of WG Pu. Specifically, 8.4 mL of 1 M HF was added to 21.45 mL of 0.098 M Pu(NO<sub>3</sub>)<sub>4</sub>(aq) to immediately yield a light pink solid that

was dried overnight under a flow of argon. To limit the effects of radiolytic decay on chemical structure, all samples were analyzed readily after their production.

### Powder X-ray Diffraction

$\text{PuF}_4$  was prepared by loading  $\sim 1$  g of powder into a 3D-printed sample holder with a  $\mu\text{m}$  thick polyimide film window. Powder X-ray diffraction data was collected using a Rigaku Ultima IV diffractometer equipped with a Cu sealed tube X-ray source and a  $5^\circ$  linear position sensitive detector on a 285 mm radius goniometer. Cu K- $\alpha$  X-rays were selected by use of a Ni filter. Diffraction data was collected from  $5$ – $159^\circ 2\theta$  in intervals of  $0.02^\circ$ . Data was analyzed using TOPAS version 6 [99].

Diffractograms of  $\text{PuF}_4\text{-xH}_2\text{O}$  were collected with a Bruker Quazar single crystal X-ray diffractometer (SC-XRD) featuring monochromated Mo K- $\alpha$  radiation. The utilization of an SC-XRD as opposed to a powder X-ray diffractometer (pXRD) led to broader diffractograms, a feature primarily attributed to the lower resolution of the SC-XRD detector. The diffractometer had a  $1024 \times 1024$  resolution and was positioned at a distance of 200 mm. Phi scans were conducted over  $360^\circ$  for a duration of up to 720 s, ranging from  $4^\circ$  to  $54^\circ 2\theta$ , and diffractograms were obtained by integrating the resulting Debye rings. Diffractograms were obtained for freshly synthesized  $\text{PuF}_4\text{-xH}_2\text{O}$  both before and after subjection to thermogravimetric analysis (TGA). To address  $2\theta$  displacement, we employed lanthanum hexaboride ( $\text{LaB}_6$ (s); Alfa Aesar, 99.5%) as an external standard. The International Centre for Diffraction Data (ICDD) database of crystal and powder X-ray diffraction [100] was used for phase matching.

### TGA

Thermogravimetric analysis (TGA) was used to provide information on  $\text{PuF}_4\text{-xH}_2\text{O}$  water content and probe chemical changes of hydrated  $\text{PuF}_4$  as a function of temperature.  $\text{PuF}_4\text{-xH}_2\text{O}$  (11.40 mg) was placed inside an alumina crucible and heated to  $800^\circ\text{C}$  at a ramp rate of  $5^\circ\text{C}/\text{min}$  and a sampling interval of 2 s/pt. A balance flow rate of 50 mL/min and a sample flow rate of 80 mL/min was used during sample measurements. Increased flow rates were used to prevent corrosion of the instrument due to release of HF during heating.

### SEM

The imaging analysis for anhydrous  $\text{PuF}_4$  was performed using a Thermo-Fisher Inc., (Hillsboro, OR) Quattro Field Emission Gun (FEG) scanning electron microscope (SEM) equipped with a circular backscattered electron (CSE) detector and an iXRF Systems (Austin, TX) X-ray energy dispersive spectroscopy (EDS) detector. The system was modified to handle radioactive materials and the vacuum pumping system of the microscope was connected to a series of high efficiency filters to prevent the release of radioactivity to the environment. A beam energy of 20 keV was effective at revealing the light elements (F-K line) and the heavy element Pu-M line efficiently. The spatial

resolution of the elemental mapping was unlikely to be better than  $1\ \mu\text{m}^2$ .

A JEOL JCM-6000 Plus Neoscope benchtop SEM was used to study the morphology of hydrated plutonium fluoride materials. Images were obtained using accelerating voltages ranging from 10 to 15 kV, with magnification reaching up to  $5000\times$  under secondary electron (SE) mode. To mitigate the hazards associated with handling dispersible plutonium, all sample materials were prepared within a negative pressure glovebox, and a minimal amount of plutonium powder was meticulously dispersed on carbon tape affixed to an aluminum stub. These stubs were tested for robustness and dispersibility then loaded out of the glovebox onto the benchtop.

### Raman Spectroscopy

Plutonium samples were contained within a double-walled containment cell containing  $\text{BaF}_2$  transmission windows for all vibrational spectroscopy and diffuse reflectance measurements. Raman and fluorescence spectra were acquired with a LabRAM HR800 (Horiba Jobin-Yvon)  $\mu$ -Raman spectrometer equipped with an Andor iDus charge coupled device (CCD) detector (DU146A-LDC-DD). The detector had a  $15\text{-}\mu\text{m}$  pixel resolution and a  $2000 \times 256$  pixel array, and most experiments were conducted by binning the spectral array by a factor of two. The detector was maintained at a temperature of  $-92^\circ\text{C}$  with the aid of a water chiller and thermoelectric cooling. Excitation wavelengths of 457, 488, 514, and 633 nm were used, and spectra were processed using bandpass filters from Semrock Inc. The laser was focused onto the sample with a  $50\times$  objective and power at the sample ranged from 100–500  $\mu\text{W}$ . Laser power was controlled by a half-wave plate and polarizer. Specular reflection from the sample was eliminated with ultra-steep, long pass edge filters produced by Semrock Inc., and an 1800 g/mm grating was used to disperse light onto the detector. Data acquisition periods ranged from 1–12 hr. Labspec 5.78 software was used to control data acquisition parameters. For each integration time, at least two additional spectra were co-added to remove cosmic ray contributions. Fluorescence measurements were recorded using a 600 g/mm grating up to 900 nm with 457, 488, and 514 nm excitation for  $\text{PuF}_4\text{-xH}_2\text{O}$  samples. Acquisition periods for fluorescence measurements lasted approximately 5 minutes. Additional post-processing, including background subtraction, peak smoothing (10-point adjacent averaging), and peak fitting were conducted in OriginPro; all peaks were assumed to have a Lorentzian line shape.

### Infrared Spectroscopy

Diffuse reflectance Fourier transform infrared spectroscopy (DRIFTS) was performed with a Continuum IR microscope coupled to a Nicolet 6700 spectrometer. A  $15\times$  Reflachromat objective from Thermo Fisher was used to focus light onto samples. A mercury cadmium telluride (MCT) detector, cooled with liquid nitrogen, was used to record the interferograms. Spectra were collected over a  $800$ – $7500\text{ cm}^{-1}$  spectral window.

with 4 cm<sup>-1</sup> resolution. The BaF<sub>2</sub> windows of the double-walled containment cell limited optical transmission to energies > 800 cm<sup>-1</sup>. A data acquisition period consisted of the average of 2000 individual spectra, and multiple measurements were taken to ensure reproducibility. Baseline correction was performed with OriginPro software.

### Diffuse Reflectance Spectroscopy

An Olympus microscope coupled to an Andor Kymera 328i scanning spectrometer was used to perform diffuse reflectance spectroscopy (DRS) measurements. Illumination was provided with an Olympus quartz tungsten halogen (QTH) lamp with a spectral range of 400–2500 nm. Light was passed through a polarizer and focused onto the sample with an Olympus 20× objective. Reflected light polarized perpendicular to the incident light was collected with the objective at normal incidence, directed to a lens, focused into a broadband fiber optic with low OH content, and then directed into the Kymera 328i spectrometer. Three spectral regions were collected that used two different detectors and three different gratings. The first spectral range, 400–900 nm, was collected with an Andor Newton (DU920P-DU2) CCD detector and a 1200 g/mm grating blazed at 500 nm. The second spectral range, 600–1200 nm, was collected with an Andor iDus InGaAs-1.7 detector and 600 g/mm grating blazed at 1000 nm. The third spectral range, 930–1600 nm, was collected with an Andor iDus InGaAs-1.7 detector and a 600 g/mm grating blazed at 1200 nm. A longpass edge filter (900 nm) was used to block visible light that could result in second order reflections and produce false signals in the InGaAs detector. The spectral resolution was 1.0 nm. The system was calibrated, across the three spectral ranges, with the 404.7, 435.8, 576.96, 579.1, 696.5, 763.5, 811.5, 866.8, 912.3, 965.8, 1047.1, 1148.8, 1211.2, 1295.7, 1331.3, 1529.9 nm lines of a HgAr lamp. Spectralon placed in the double-walled cell was used to collect a reference spectrum, and Andor Solis software was used to collect absorption data. The three regions were then stitched together to construct the spectrum. Manual adjustments to the absorbance were unnecessary.

### Author contributions

**Jared S. Kinyon:** Writing - original draft, Writing – review and editing, Visualization. **Eliel Villa-Aleman:** - Writing - original draft, Writing – review and editing, Data Curation, Conceptualization. **Elodia Ciprian:** Writing – review and editing, Data Curation. **Amy E. Hixon:** Writing – review and editing, Resources. **Bryan J. Foley:** Writing – review and editing, Resources. **Jonathan H. Christian:** Writing – review and editing, Funding acquisition, Project administration, Conceptualization, Resources. **Jason R. Darvin:** Writing – review and editing, Data Curation, Investigation. **Don D. Dick:** Writing – review and editing, Data Curation. **Amanda J. Casella:** Writing – review and editing, Resources. **Lucas E. Sweet:** Writing – review and editing, visualization, Data Curation, Formal Analysis. **Edgar C. Buck:** Writing – review and editing, Data Curation, Investigation. **Forrest D. Heller:** Writing – review and editing. **Aaron D. Nicholas:** Writing – review and editing. **Cody A. Nizinski:** Writing – review and editing, Data

Curation, Investigation. **Richard A. Clark:** Writing – review and editing.

### Conflicts of interest

There are no conflicts to declare.

### Data availability

Detailed datasets, including raw data and processed results, are available from the corresponding author upon reasonable request.

### Acknowledgements

This work was funded by the Office of Defense Nuclear Nonproliferation Research and Development within the U.S. Department of Energy's National Nuclear Security Administration for the synthesis of PuF<sub>4</sub> and material characterization. This work was produced by Battelle Savannah River Alliance, LLC under Contract No. 89303321CEM000080 and/or a predecessor contract with the U.S. Department of Energy. Publisher acknowledges the U.S. Government license to provide public access under the DOE Public Access Plan (<http://energy.gov/downloads/doe-public-access-plan>). The United States Government retains and the publisher, by accepting this article for publication, acknowledges that the United States Government retains a non-exclusive, paid-up, irrevocable, worldwide license to publish or reproduce the published form of this work, or allow others to do so, for United States Government purposes.

### Notes and references

1. Johns, I.B. and G.H. Moulton, *Large-scale Preparation of the Anhydrous Fluorides of Plutonium*. Report LA-193, Los Alamos Scientific Laboratory, Los Alamos, NM, 1944.
2. Baker, R.D., *Preparation of plutonium metal by the bomb method*. Report LA-473, Los Alamos Scientific Laboratory, 1946.
3. Conner, W.V., *Process studies on the reduction of plutonium tetrafluoride to metal*. 1966, Rocky Flats Div., Dow Chemical Co., Golden, Colo.
4. Moser, W.S. and J.D. Navratil, *Review of major plutonium pyrochemical technology*. Journal of the Less Common Metals, 1984. **100**: p. 171-187.
5. Johns, I.B., *Equilibrium Constants and Heats of Reaction for the Hydrofluorination of Uranium Dioxide and Plutonium Dioxide*. 1945: United States.
6. Clark, D.L., et al., *Plutonium*. 2006: Springer.
7. Le Guellec, M., et al., *Grain size analysis and characterization by Raman spectroscopy of a homogeneous sintered MOX fuel*. Journal of the European Ceramic Society, 2022. **42**(16): p. 7553-7560.
8. Talip, Z., et al., *Characterization of un-irradiated MIMAS MOX fuel by Raman spectroscopy and EPMA*. Journal of Nuclear Materials, 2018. **499**: p. 88-97.

9. Jegou, C., et al., *Raman micro-spectroscopy of UOX and MOX spent nuclear fuel characterization and oxidation resistance of the high burn-up structure*. *Journal of Nuclear Materials*, 2015. **458**: p. 343-349.

10. Worley, C.G. and G.J. Havrilla, *Micro-X-ray Fluorescence Characterization of Mixed Oxide Fuel Surrogate Feed Material*. *Analytical Chemistry*, 1998. **70**(14): p. 2957-2963.

11. Abram, T. and S. Ion, *Generation-IV nuclear power: A review of the state of the science*. *Energy Policy*, 2008. **36**(12): p. 4323-4330.

12. *Status and Advances in MOX Fuel Technology*, series= *Technical Reports Series*. 2003.

13. Tandon, L., *Radiolysis of Salts and Long-Term Storage Issues for Both Pure and Impure PuO<sub>2</sub> Materials in Plutonium Storage Containers*. 2000: United States.

14. Hobart, D.E., et al. *Formation, characterization, and stability of plutonium (IV) colloid; A progress report*. 1989. United States.

15. Carnall, W.T., et al., *Analysis of the crystal-field spectra of the actinide tetrafluorides. I. UF<sub>4</sub>, NpF<sub>4</sub>, and PuF<sub>4</sub>*. *The Journal of Chemical Physics*, 1991. **95**(10): p. 7194-7203.

16. Kern, S., et al., *Temperature variation of the structural parameters in actinide tetrafluorides*. *The Journal of Chemical Physics*, 1994. **101**(11): p. 9333-9337.

17. Capan, C., et al., *Probing the Pu<sup>4+</sup> magnetic moment in PuF<sub>4</sub> with <sup>19</sup>F NMR spectroscopy*. *Physical Review B*, 2016. **93**(22): p. 224409.

18. McCoy, K., et al., *Radiation damage and annealing in plutonium tetrafluoride*. *Journal of Nuclear Materials*, 2017. **496**: p. 379-387.

19. Wayne, D.M., et al., *X-ray diffraction, differential scanning calorimetry and evolved gas analysis of aged plutonium tetrafluoride (PuF<sub>4</sub>)*. *Journal of Radioanalytical and Nuclear Chemistry*, 2021. **329**(2): p. 741-756.

20. Walter, E.D., et al., *Measurement of local magnetic fields in actinide tetrafluorides*. *The Journal of Chemical Physics*, 2021. **154**(21): p. 211101.

21. Casella, A.J., et al., *In Stream Monitoring of Off-Gasses from Plutonium Fluorination*. *Actinide Research Quarterly, 2019. Second Quarter 2019*.

22. Cox, L.E. and J.D. Farr, *4f binding-energy shifts of the light-actinide dioxides and tetrafluorides*. *Physical Review B*, 1989. **39**(15): p. 11142-11145.

23. Miskowiec, A., et al., *Vibrational properties of uranium fluorides*. *Physica B: Condensed Matter*, 2019. **570**: p. 194-205.

24. Villa-Aleman, E. and M.S. Wellons, *Characterization of uranium tetrafluoride (UF<sub>4</sub>) with Raman spectroscopy*. *Journal of Raman Spectroscopy*, 2016. **47**(7): p. 865-870.

25. Gans, P., B.J. Hathaway, and B.C. Smith, *Diffuse reflectance spectra of some uranium (IV) complexes*. *Spectrochimica Acta*, 1965. **21**(9): p. 1589-1595.

26. Khanaev, E.I., E.G. Teterin, and L.A. Luk'yanova, *IR spectroscopic study of dehydration products of UF<sub>4</sub> and PuF<sub>4</sub> crystal hydrates in an anhydrous HF current*. *Journal of Applied Spectroscopy*, 1967. **6**(6): p. 533-538.

27. DeVore, M.A., et al., *Vibrational spectroscopy of uranium tetrafluoride hydrates*. *Vibrational Spectroscopy*, 2021. **115**: p. 103277.

28. Foley, B.J., et al., *Probing the hydrolytic degradation of UF<sub>4</sub> in humid air*. *Dalton Transactions*, 2022. **51**(15): p. 6061-6067.

29. Ghosh, S.N., W. Gordy, and D.G. Hill, *Paramagnetic Resonance in Uranium Salts*. *Physical Review*, 1954. **96**(1): p. 36-38.

30. Teterin, A.Y., et al., *Electronic structure of solid uranium tetrafluoride UF<sub>4</sub>*. *Physical Review B*, 2006. **74**(4): p. 045101.

31. Christian, J.H., et al., *Characterizing the solid hydrolysis product, UF<sub>4</sub>(H<sub>2</sub>O)<sub>2.5</sub>, generated from neat water reactions with UF<sub>4</sub> at room temperature*. *Dalton Transactions*, 2021. **50**(7): p. 2462-2471.

32. Villa-Aleman, E., et al., *Raman microspectroscopy of PuO<sub>2</sub> particulate aggregates*. *Journal of Nuclear Materials*, 2019. **515**: p. 140-149.

33. Villa-Aleman, E., et al., *Raman spectroscopy: A tool to investigate alpha decay damage in a PuO<sub>2</sub> crystal lattice and determining sample age since calcination*. *Journal of Raman Spectroscopy*, 2019. **50**(6): p. 899-901.

34. Villa-Aleman, E., et al., *Raman signatures from age-dating PuO<sub>2</sub> since last calcination*. *Journal of Nuclear Materials*, 2021. **551**: p. 152969.

35. Villa-Aleman, E., et al., *The electronic Raman scattering spectrum of PuO<sub>2</sub>*. *Journal of Raman Spectroscopy*, 2023. **54**(3): p. 324-332.

36. Villa-Aleman, E., et al., *Laser-induced annealing of aged PuO<sub>2</sub>*. *Journal of Raman Spectroscopy*, 2021. **52**(8): p. 1486-1489.

37. Villa-Aleman, E., et al., *Diffuse Reflectance Spectroscopy and Principal Component Analysis to Retrospectively Determine Production History of Plutonium Dioxide*. *Applied Spectroscopy*, 2022. **77**(5): p. 449-456.

38. Christian, J.H., et al., *Raman and infrared spectra of plutonium (IV) oxalate and its thermal degradation products*. *Journal of Nuclear Materials*, 2022. **562**: p. 153574.

39. Christian, J.H., et al., *Probing the thermal decomposition of plutonium (III) oxalate with IR and Raman spectroscopy, X-ray diffraction, and electron microscopy*. *Journal of Nuclear Materials*, 2023. **584**: p. 154596.

40. Vigier, N., et al., *Reaction mechanisms of the thermal conversion of Pu(IV) oxalate into plutonium oxide*. *Journal of Alloys and Compounds*, 2007. **444-445**: p. 594-597.

41. Teterin, Y.A., et al., *Electronic structure and chemical bonding in PuO<sub>2</sub>*. *Physical Review B*, 2013. **87**(24): p. 245108.

42. Karelina, A., et al., *Thermal decomposition of Np(IV) and Pu(III, IV) oxalates*. *Journal of Radioanalytical and Nuclear Chemistry*, 1990. **143**(1): p. 241-252.

43. Vitova, T., et al., *Exploring the electronic structure and speciation of aqueous and colloidal Pu with high energy resolution XANES and computations*. *Chemical Communications*, 2018. **54**(91): p. 12824-12827.

44. Bagus, P.S., B. Schacherl, and T. Vitova, *Computational and Spectroscopic Tools for the Detection of Bond Covalency in Pu(IV) Materials*. *Inorganic Chemistry*, 2021. **60**(21): p. 16090-16102.

45. Isbill, S.B., et al., *Computational insights into the lattice dynamics of Pu(IV) oxalates*. *Journal of Nuclear Materials*, 2023. **573**: p. 154106.

46. Wedal, J.C., F. Furche, and W.J. Evans, *Density Functional Theory Analysis of the Importance of Coordination Geometry for 5f<sup>3</sup>6d<sup>1</sup> versus 5f<sup>4</sup> Electron Configurations in*

U(II) Complexes. *Inorganic Chemistry*, 2021. **60**(21): p. 16316-16325.

47. South, C.J. and L.E. Roy, *Insights into the thermal decomposition of plutonium(IV) oxalate – a DFT study of the intermediate structures*. *Journal of Nuclear Materials*, 2021. **549**: p. 152864.

48. Pepper, M. and B.E. Bursten, *The electronic structure of actinide-containing molecules: a challenge to applied quantum chemistry*. *Chemical Reviews*, 1991. **91**(5): p. 719-741.

49. Krupa, J.C., *Optical excitations in lanthanide and actinide compounds*. *Journal of Alloys and Compounds*, 1995. **225**(1): p. 1-10.

50. Larson, A.C., R.B. Roof Jnr, and D.T. Cromer, *The crystal structure of UF<sub>4</sub>*. *Acta Crystallographica*, 1964. **17**(5): p. 555-558.

51. Keenan, T.K. and L.B. Asprey, *Lattice constants of actinide tetrafluorides including berkelium*. *Inorganic Chemistry*, 1969. **8**(2): p. 235-238.

52. Asprey, L.B. and R.G. Haire, *On the actinide tetrafluoride lattice parameters*. *Inorganic and Nuclear Chemistry Letters*, 1973. **9**(11): p. 1121-1128.

53. Zachariasen, W.H., *Crystal chemical studies of the 5f-series of elements. XII. New compounds representing known structure types*. *Acta Crystallographica*, 1949. **2**(6): p. 388-390.

54. Shannon, R., *Revised effective ionic radii and systematic studies of interatomic distances in halides and chalcogenides*. *Acta Crystallographica Section A*, 1976. **32**(5): p. 751-767.

55. Dawson, J.K., R.W.M. D'Eye, and A.E. Truswell, *The hydrated tetrafluorides of uranium and plutonium*. *Journal of the Chemical Society (Resumed)*, 1954(0): p. 3922-3929.

56. Dawson, J.K., et al., *The preparation and some properties of plutonium fluorides*. *Journal of the Chemical Society (Resumed)*, 1954(0): p. 558-564.

57. Zachariasen, W.H., U.S.A.E. Commission, and L. Argonne National, *X-ray diffraction studies of fluorides of plutonium and neptunium: chemical identity and crystal structure*. United States. Atomic Energy Commission. MDDC ;1396. 1947, Oak Ridge, Tenn.: Atomic Energy Commission. 16 p.

58. Gagarinskii, Y.V., et al., *The crystal hydrate UF<sub>4</sub>·4/3 H<sub>2</sub>O*. Soviet Atomic Energy, 1965. **18**(1): p. 43-48.

59. Pastoor, K.J., et al., *Structural Characterization of Uranium Tetrafluoride Hydrate (UF<sub>4</sub>·2.5H<sub>2</sub>O)*. *The Journal of Physical Chemistry C*, 2022. **126**(31): p. 13256-13267.

60. Borisov, S.V. and G.M. Zadneprovskii, *The crystal structure of UF<sub>4</sub>·2.5H<sub>2</sub>O*. Soviet Atomic Energy, 1971. **31**(1): p. 761-763.

61. Mandleberg, C.J. and K.E. Francis, *The solubility of PuF<sub>4</sub> in Nitric acid solutions and the solubility product of PuF<sub>4</sub>*. 1952: United Kingdom.

62. Moseley, J.D. and R.O. Wing, *Properties of plutonium dioxide*. 1965, Rocky Flats Div., Dow Chemical Co., Denver, Colo.

63. Machuron-Mandard, X. and C. Madic, *Plutonium dioxide particle properties as a function of calcination temperature*. *Journal of Alloys and Compounds*, 1996. **235**(2): p. 216-224.

64. Myers, M.N., *Thermal decomposition of plutonium (IV) oxalate and hydrofluorination of plutonium (IV) oxalate and oxide*. 1956, General Electric Co. Hanford Atomic Products Operation, Richland, Wash.

65. Smith, P.K., et al., *Effect of oxalate precipitation on PuO<sub>2</sub> microstructures*. 1976: United States. p. 11.

66. Chudinov, E.a.C.D.Y., *Atomnaya Energiya*, 1970. **28**: p. 151-153.

67. Goldstein, M., R.J. Hughes, and W.D. Unsworth, *Vibrational spectra of some heavy metal tetrafluorides in the solid state*. *Spectrochimica Acta Part A: Molecular Spectroscopy*, 1975. **31**(5): p. 621-624.

68. Roodenko, K., et al., *Modified phonon confinement model for Raman spectroscopy of nanostructured materials*. *Physical Review B*, 2010. **82**(11): p. 115210.

69. Corbey, J.F., et al., *Quantitative Microstructural Characterization of Plutonium Oxalate Auto-Degradation and Evidence for PuO<sub>2</sub> Nanocrystal Formation*. *European Journal of Inorganic Chemistry*, 2021. **2021**(32): p. 3277-3291.

70. Hudry, D., et al., *Ultra-Small Plutonium Oxide Nanocrystals: An Innovative Material in Plutonium Science*. *Chemistry – A European Journal*, 2014. **20**(33): p. 10431-10438.

71. Pointurier, F., C. Lelong, and O. Marie, *Study of the chemical changes of μ-sized particles of uranium tetrafluoride (UF<sub>4</sub>) in environmental conditions by means of micro-Raman spectrometry*. *Vibrational Spectroscopy*, 2020. **110**: p. 103145.

72. Toth, L.M. and H.A. Friedman, *The IR spectrum of Pu(IV) polymer*. *Journal of Inorganic and Nuclear Chemistry*, 1978. **40**(5): p. 807-810.

73. Arab-Chapelet, B., et al., *Synthesis and characterization of mixed An(IV)An(III) oxalates (An(IV)=Th, Np, U or Pu and An(III)=Pu or Am)*. *Journal of Nuclear Materials*, 2008. **373**(1): p. 259-268.

74. Bryan, S.A., et al., *Spectroscopic monitoring of spent nuclear fuel reprocessing streams: an evaluation of spent fuel solutions via Raman, visible, and near-infrared spectroscopy*. 2011. **99**(9): p. 563-572.

75. Armstrong, D.P., W.D. Bostick, and W.H. Fletcher, *An FT-IR Study of the Atmospheric Hydrolysis of Uranium Hexafluoride*. *Applied Spectroscopy*, 1991. **45**(6): p. 1008-1016.

76. Wagner, G.L., et al., *Morphologic and chemical characterization of products from hydrolysis of UF<sub>6</sub>*. *Journal of Fluorine Chemistry*, 2015. **178**: p. 107-114.

77. Kirkegaard, M.C., et al., *Formation of a uranyl hydroxide hydrate via hydration of [(UO<sub>2</sub>F<sub>2</sub>)(H<sub>2</sub>O)]<sub>7</sub>·4H<sub>2</sub>O*. *Dalton Transactions*, 2019. **48**(36): p. 13685-13698.

78. Ohwada, K., *Uranium-fluorine lattice vibration of uranyl fluoride*. *Journal of Inorganic and Nuclear Chemistry*, 1971. **33**(6): p. 1615-1623.

79. Thomas, R.K. and H.W. Thompson, *Hydrogen bonding in the vapour phase between water and hydrogen fluoride: the infrared spectrum of the 1:1 complex*. *Proceedings of the Royal Society of London. A. Mathematical and Physical Sciences*, 1997. **344**(1639): p. 579-592.

80. Lohr, J.E. and G. Kortüm, *Reflectance Spectroscopy: Principles, Methods, Applications*. 2012: Springer Berlin Heidelberg.

81. Krupa, J.C. and W.T. Carnall, *Electronic structure of U<sup>4+</sup>, Np<sup>4+</sup>, and Pu<sup>4+</sup> doped into ThSiO<sub>4</sub> single crystal*. *The Journal of Chemical Physics*, 1993. **99**(11): p. 8577-8584.

## ARTICLE

## Journal Name

82. Liu, G.K., et al., *Analysis of the crystal-field spectra of the actinide tetrafluorides. II. AmF<sub>4</sub>, CmF<sub>4</sub>, Cm<sup>4+</sup>:CeF<sub>4</sub>, and Bk<sup>4+</sup>:CeF<sub>4</sub>*. The Journal of Chemical Physics, 1994. **101**(10): p. 8277-8289.

83. Hobart, D.E. and K. Boland, *Diffuse Reflectance Spectroscopy of Plutonium Solids*. Actinide Res. Quart, 2011. **2**: p. 37-41.

84. Matonic, J.H., B.L. Scott, and M.P. Neu, *High-Yield Synthesis and Single-Crystal X-ray Structure of a Plutonium(III) Aquo Complex: [Pu(H<sub>2</sub>O)<sub>9</sub>][CF<sub>3</sub>SO<sub>3</sub>]<sub>3</sub>*. Inorganic Chemistry, 2001. **40**(12): p. 2638-2639.

85. Runde, W., et al., *Synthesis and structural characterization of a molecular plutonium(iv) compound constructed from dimeric building blocks*. Chemical Communications, 2007(17): p. 1728-1729.

86. Runde, W., et al., *Directed Synthesis of Crystalline Plutonium(III) and (IV) Oxalates: Accessing Redox-Control Separations in Acidic Solutions*. Inorganic Chemistry, 2009. **48**(13): p. 5967-5972.

87. Reilly, S.D., B.L. Scott, and A.J. Gaunt, *[N(n-Bu)<sub>4</sub>]<sub>2</sub>[Pu(NO<sub>3</sub>)<sub>6</sub>] and [N(n-Bu)<sub>4</sub>]<sub>2</sub>[PuCl<sub>6</sub>]: Starting Materials To Facilitate Nonaqueous Plutonium(IV) Chemistry*. Inorganic Chemistry, 2012. **51**(17): p. 9165-9167.

88. Reilly, S.D., et al., *Synthesis and characterization of NpCl<sub>4</sub>(DME)<sub>2</sub> and PuCl<sub>4</sub>(DME)<sub>2</sub> neutral transuranic An(IV) starting materials*. Dalton Transactions, 2014. **43**(4): p. 1498-1501.

89. Minasian, S.G., et al., *Synthesis and Structure of (Ph<sub>4</sub>P)<sub>2</sub>MCl<sub>6</sub> (M = Ti, Zr, Hf, Th, U, Np, Pu)*. Inorganic Chemistry, 2012. **51**(10): p. 5728-5736.

90. Rosario-Amorin, D., et al., *Synthesis and Coordination Chemistry of Phosphine Oxide Decorated Dibenzofuran Platforms*. Inorganic Chemistry, 2012. **51**(12): p. 6667-6681.

91. Reilly, S.D., et al., *Plutonium(iv) complexation by diglycolamide ligands—coordination chemistry insight into TODGA-based actinide separations*. Chemical Communications, 2012. **48**(78): p. 9732-9734.

92. Matonic, J.H., et al., *Synthesis and crystal structure of a ten-coordinate plutonium(IV) ion complexed by 2-[(diphenylphosphino)methyl]pyridine N,P-dioxide: [Pu(NO<sub>3</sub>)<sub>3</sub>{2-[(C<sub>6</sub>H<sub>5</sub>)<sub>2</sub>P(O)CH<sub>2</sub>]C<sub>5</sub>H<sub>4</sub>NO<sub>2</sub>}][Pu(NO<sub>3</sub>)<sub>6</sub>]<sub>0.5</sub>*. Journal of the Chemical Society, Dalton Transactions, 2002(11): p. 2328-2332.

93. Nikitenko, S.I. and P. Moisy, *Formation of Higher Chloride Complexes of Np(IV) and Pu(IV) in Water-Stable Room-Temperature Ionic Liquid [BuMeIm][Tf<sub>2</sub>N]*. Inorganic Chemistry, 2006. **45**(3): p. 1235-1242.

94. Hess, R.F., et al., *Synthesis and Structural Characterization of the First Quaternary Plutonium Thiophosphates: K<sub>3</sub>Pu(PS<sub>4</sub>)<sub>2</sub> and APuP<sub>2</sub>S<sub>7</sub> (A = K, Rb, Cs)*. Journal of the American Chemical Society, 2002. **124**(7): p. 1327-1333.

95. Zhang, Y., E.R. Vance, and T. McLeod, *Diffuse reflectance spectroscopy of Np and Pu in zirconia and pyrochlore-structured Y<sub>2</sub>Ti<sub>2</sub>O<sub>7</sub>*. Journal of Nuclear Materials, 2012. **420**(1): p. 278-281.

96. Zhang, Y. and E.R. Vance, *Diffuse reflectance spectroscopy of tetravalent neptunium and plutonium ions in ThO<sub>2</sub>*. Journal of Nuclear Materials, 2008. **374**(1): p. 192-196.

97. Gregg, D.J., et al., *The incorporation of plutonium in lanthanum zirconate pyrochlore*. Journal of Nuclear Materials, 2013. **443**(1): p. 444-451.

98. Zhang, Y. and E.R. Vance, *Plutonium in monazite and brabantite: Diffuse reflectance spectroscopy study*. Journal of Nuclear Materials, 2008. **375**(3): p. 311-314.

99. TOPAS, *Bruker AXS software package Copyright 1999. 2016*.

100. Gates-Rector, S. and T. Blanton, *The Powder Diffraction File: a quality materials characterization database*. Powder Diffraction, 2019. **34**(4): p. 352-360.